PHYSICAL REVIEW FLUIDS **2**, 031601(R) (2017)

Droplet depinning in a wake

Alireza Hooshanginejad and Sungyon Lee*
Department of Mechanical Engineering, Texas A&M University, College Station, Texas 77843, USA
(Received 16 May 2016; published 8 March 2017)

Pinning and depinning of a windswept droplet on a surface is familiar yet deceptively complex for it depends on the interaction of the contact line with the microscopic features of the solid substrate. This physical picture is further compounded when wind of the Reynolds number greater than 100 blows over pinned drops, leading to the boundary layer separation and wake generation. In this Rapid Communication, we incorporate the well-developed ideas of the classical boundary layer to study partially wetting droplets in a wake created by a leader object. Depending on its distance from the leader, the droplet is observed to exhibit drafting, upstream motion, and splitting, due to the wake-induced hydrodynamic coupling that is analogous to drafting of moving bodies. We successfully rationalize the onset of the upstream motion regime using a reduced model that computes the droplet shape governed by the pressure field inside the wake.

DOI: 10.1103/PhysRevFluids.2.031601

Bodies moving through a fluid in a high Reynolds number regime experience hydrodynamic coupling when their wakes interact with each other [1]. As a seminal example, hydrodynamic drafting reduces the drag of an object (follower) when it is placed in the wake of another object (leader) [2]. More complex wake-induced behaviors [3–6] emerge when objects flap or deform with the flow. For instance, in the case of a deformable leader-follower pair, surprisingly, the leader object experiences reduced drag instead of the follower, referred to as inverted drafting [6]. A passive flapping follower behind a solid leader can even extract energy from the Kármán vortex street to move upstream towards the leader without expending energy of its own [3,4].

While most studies of this nature look for inspiration in biological systems, hydrodynamic coupling effects may also be present in a completely different yet familiar situation: droplets pinned or running on the surface of a fast-moving vehicle. A partially wetting drop is able to remain in place against external forcing due to contact angle hysteresis that stems from the contact line pinning [7,8]. Pinning and dislodging of droplets on surfaces are relevant for aircraft icing [9,10], atomized lubrication in micromachining [11], and heat exchangers [12]. Due to its familiarity and practical implications, pinning of a single droplet on a solid substrate has been studied extensively in the low Reynolds number regime [7,8,13–17] and, to a lesser extent, in the inertia-driven regime [18–20].

In this present work, we use wind-tunnel experiments to study the wake-induced behavior of a partially wetting droplet (follower) in the wake of a fixed solid protuberance (leader). This is a first step towards understanding the coordinated behavior of multiple droplets in wind without the complexity of a deformable leader. Analogous to the conventional hydrodynamic drafting [2], when the wind blows over a drop pinned behind a leader solid, the droplet experiences reduced drag and takes off at higher imposed wind. However, as the droplet's distance from the solid is varied, more complex and surprising droplet behaviors emerge. By coupling the knowledge of wake behind a rigid bluff body [21–28] and a deformable body (i.e., bubble) [29–33] with droplet pinning [7,8], we develop a reduced model that focuses on the onset of droplet motion and qualitatively captures the experimental results. The combination of the boundary layer and droplet dynamics represents analytical tools to explore fundamental problems at the intersection of the two fields.

We experimentally measure the critical air velocity, U_c, at which a water droplet *depins* from the substrate in the wake of a leading object inside the test section (2.5 cm tall and 5.1 cm wide)

*sungyon.lee@tamu.edu

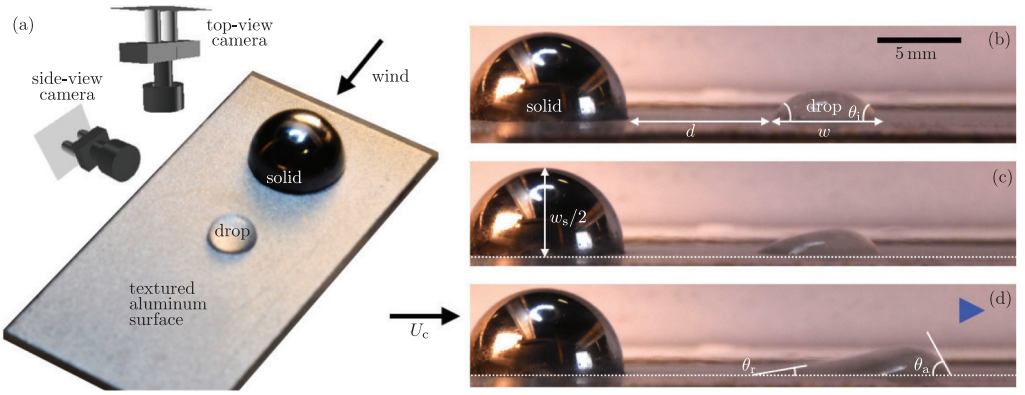

FIG. 1. (a) A water droplet is placed behind a steel hemispherical protuberance on a textured aluminum surface inside a miniature wind tunnel. The images from top-view and side-view cameras are used to analyze the evolving droplet shapes and to determine the onset of motion. (b) A typical side-view image of a droplet ($V = 50\ \mu$L) placed at a distance, d, downstream from the solid: With no external forcing, the droplet of width, w, forms $\theta_i = 49.1^\circ$ with the textured surface. (c) When the wind is turned on, the droplet visibly deforms asymmetrically in the direction of the wind. (d) The droplet at the onset of depinning at the critical wind velocity, U_c: The drop forms the maximum contact angle, $\theta_a = 63.5^\circ$, on the advancing side and the minimum angle, $\theta_r = 8.2^\circ$, on the trailing edge.

of a miniature wind tunnel [20]. The leading object is a steel hemisphere with a base width, $w_s = 11.4$ mm, attached to a textured aluminum substrate with characteristic roughness of 3.26 μm. The wind tunnel generates uniform wind up to 25 m/s and forms a laminar boundary layer on the textured substrate, which is measured to be much thinner than $w_s/2$ by the time it reaches the hemisphere in the current setup [20]. When the growing boundary layer interacts with the solid hemisphere, it separates and generates wakes downstream from the hemisphere, as described in detail in [21]. In addition, the ratio of w_s to the test section width is less than 25%, ensuring that the side walls do not influence the wake [34].

Distilled water drops of varying volumes, V, are placed downstream along the centerline of the solid protrusion, and their motion is captured by the top-view and side-view cameras [Fig. 1(a)]. Initially, an axisymmetric drop forms a static contact angle of $\theta_i = 49.1^\circ$ with the substrate, as shown in Fig. 1(b). The initial distance between the trailing edge of the solid and the leading edge of the droplet is given by d. When the wind velocity, U, turns on and gradually increases, the droplet deforms asymmetrically [see Fig. 1(c)], and the downwind side of the drop forms the maximum contact angle, $\theta_a = 63.5^\circ$, and advances downstream, while the trailing edge remains pinned. At $U = U_c$, the contact angle on the trailing side reaches the minimum value, $\theta_r = 8.2^\circ$, prior to detaching from the surface. Hence, the formation of θ_a and θ_r characterizes the onset of droplet depinning [Fig. 1(d)].

Distinct from windswept droplets with no leader protrusion, the droplet behavior in the present study depends on the drop's distance from the solid, d, as well as its volume, V. For instance, beyond a critical distance from the solid, d_c, the droplet no longer feels the effects of the wake, or $U_c/U_{c0} \approx 1$ for $d \geqslant d_c$, where U_{c0} refers to the critical depinning velocity with no solid. From our experimental data shown in Fig. 2(a), $d_c \approx 1.4 w_s$ for all drops considered in the current Reynolds number range, i.e., $\mathrm{Re} \equiv U w_s/\nu_a = 2500$–$10\,000$, where ν_a is the kinematic viscosity of air. Here, d_c is set to be the distance at which U_c deviates from the corresponding value of U_{c0} by 3%. Though wake characteristics generally depend on the Reynolds number, the Re-independent behavior of d_c suggests the wakes generated behind the hemisphere do not change significantly in the Reynolds number range of our experiments, which matches the experimental findings of [21].

As the droplet is placed closer to the solid, drafting effects require stronger wind to dislodge it from the surface, or $U_c/U_{c0} > 1$ for $d < d_c$ [Fig. 2(a)]. Surprisingly, at $d/w_s \lesssim 0.4$, small droplets

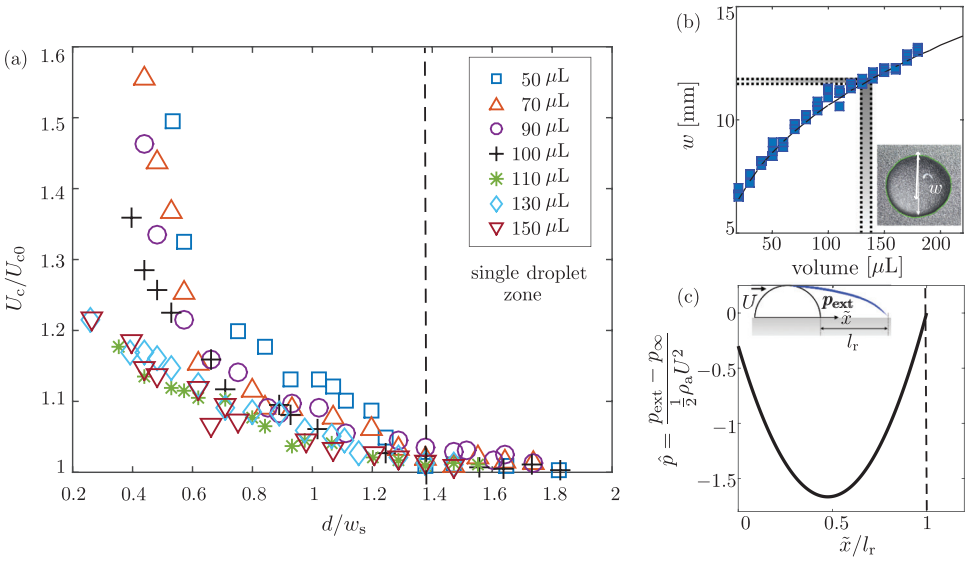

FIG. 2. (a) U_c/U_{c0} as a function of d/w_s for V ranging from 50 μL to 150 μL: U_c and U_{c0} correspond to the critical wind velocity at which a droplet depins downstream behind and without the solid, respectively. (b) The drop's initial width, w, as a function of V: Solid squares refer to experimental values of w extracted from the top-down images (inset), while the solid line is the analytic solution based on the spherical cap geometry, $w = \frac{2V^{1/3}}{\tan(\theta_i/2)}[\frac{6\sin^2(\theta_i/2)}{\pi(2+\cos\theta_i)}]^{1/3}$, with $\theta_i = 49.1°$. The shaded region indicates the transitional droplets (V = 130–140 μL) whose $w \approx l_r$, where l_r is the reattachment length. (c) The parabolic function (solid line) empirically describes the pressure inside the reattachment zone of length, l_r.

(i.e., 50–130 μL) *reverse* their direction of motion and move towards the solid against incoming wind [Figs. 3(biii)–3(biv)]. While similar upstream motion has been observed in dead fish that exhibit wake-induced synchronized flapping [4], the drop's motion is primarily governed by the low-pressure zone behind the solid. The laminar boundary layer from the wind separates on the protrusion; the pressure in the separated flow, p_{ext}, is less than the outer pressure, p_∞, forming a

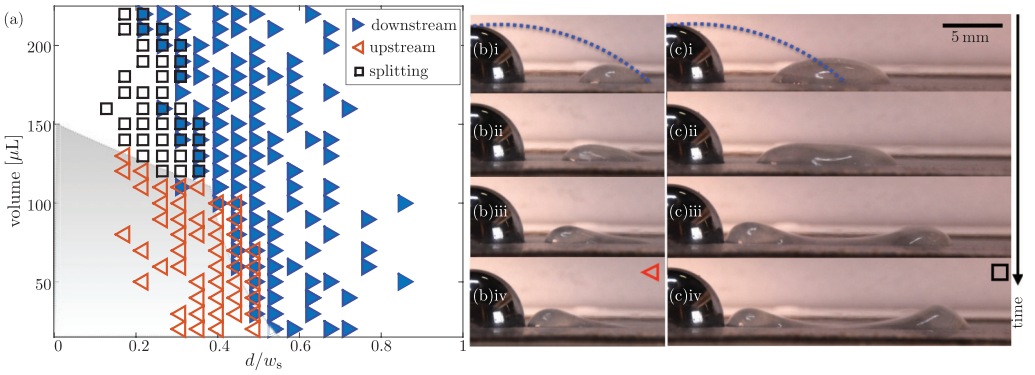

FIG. 3. (a) A V-d/w_s phase diagram summarizes distinct droplet behaviors: "downstream" (filled triangle), "upstream" (open triangle), and "splitting" (square); the shaded region corresponds to the upstream regime. (b)i–(b)iv A droplet of 50 μL depins *upstream* when it is located inside the reattachment zone behind the solid protrusion. (c)i–(c)iv A droplet of 150 μL *splits* when its downstream portion intersects the reattaching flow, while the upstream portion lies inside the separated zone.

suction region downstream from the solid. The low pressure causes the streamlines to curve inwards and reattach to the substrate at the reattachment point [21]. Hence, the droplet inside the reattachment zone is "shielded" from the external wind and moves towards the low-pressure region. In the current Reynolds number range, it is reasonable to assume that the length of this zone, l_r, must correspond to w_s, the diameter of the hemisphere [21,25].

Then, what must happen if the droplet is placed at the reattachment point? Specifically, large drops (i.e., 110–220 μL) that "intersect" the reattaching flow (i.e., $d/w_s \lesssim 0.2$) are observed to *split* into two drops that move in opposite directions. This can be explained by considering that pressure at the reattachment point is at a local maximum as a stagnant point in the flow, which creates a negative curvature on the droplet surface based on the Young-Laplace equation. From this reattachment point, the droplet surface deforms in both directions (upstream and downstream) to adapt to the spatially decreasing external pressure inside the wake. As the pressure scales as $\rho_a U^2$ (where ρ_a is the air density), droplet deformations become more pronounced with the increasing velocity, which eventually leads to droplet splitting. The time evolution in the droplet shape is clearly demonstrated in Figs. 3(ciii) and 3(civ). Interestingly, splitting behavior is never observed for drops smaller than 100 μL for which surface tension effects may dominate.

If only drops that completely lie inside the reattachment zone move upstream, then drops that are too large to fit inside the zone (i.e., $w > l_r \approx w_s$) will always split and never move upstream even at small d. In fact, drops larger than 130 μL never move towards the protuberance without splitting, as shown in a V-d/w_s phase diagram in Fig. 3(a). Based on the geometry of a spherical cap with the contact angle, $\theta_i = 49.1^\circ$, the width of the smallest drop (i.e., $V = 130$–140 μL) that exhibits no upstream motion can be computed as

$$w = \frac{2V^{1/3}}{\tan(\theta_i/2)}\left[\frac{6\sin^2(\theta_i/2)}{\pi(2+\cos\theta_i)}\right]^{1/3} \approx 11.1\text{–}11.3 \text{ mm}, \tag{1}$$

which matches the solid protrusion width, $w_s = 11.4$ mm; this threshold droplet width is also experimentally measured and validated in Fig. 2(b). However, the exact nature of coupling between the droplet and the reattaching flow remains the topic of further study.

In order to rationalize the boundaries of the upstream regime in Fig. 3(a), we hereby present a reduced two-dimensional (2D) model that identifies the *largest* droplet that moves upstream at a given distance from the solid. Based on experimental observations, we assume that a droplet that moves upstream must be placed inside the reattachment zone of length, l_r. As shown in the schematic [Fig. 4(a)], we focus on a droplet of unknown height, $h(x)$, at the critical onset of motion towards the protuberance. Previously, Durbin computed the shape of a windswept, 2D slender drop at the critical depinning onset with no solid protrusion, by coupling the droplet dynamics and external pressure based on potential flow theory [16]. Distinct from the previous analysis, we presently assume that the presence of the droplet has negligible effects on both the external pressure inside the wake and the reattachment point. This is a reasonable starting point, given the complexity of the unsteady flow inside the wake that can no longer be modeled as potential flow.

In the present analysis, the drop's position relative to the solid inside the reattachment zone is a key input parameter. In order to ensure that the resultant droplet corresponds to the *largest* droplet that is completely immersed inside the reattachment zone, we fix the drop's trailing edge to match the reattachment point, while its leading edge is at a distance, $d_f \geqslant 0$, from the solid [see Fig. 4(a)]. Furthermore, the onset of upstream motion is defined in two ways. Case I: The advancing side of the drop forms the maximum contact angle, θ_a, while the receding edge forms θ_r. Case II: The drop elongates and reaches the solid (i.e., $d_f = 0$) before the receding angle has reached its minimum value.

Based on the Young-Laplace equation, the pressure inside the drop, p_i, is given by

$$p_i = p_{ext}(x) - \sigma\frac{h''(x)}{(1+h'(x)^2)^{3/2}} + \rho_w g[h(x) - y], \tag{2}$$

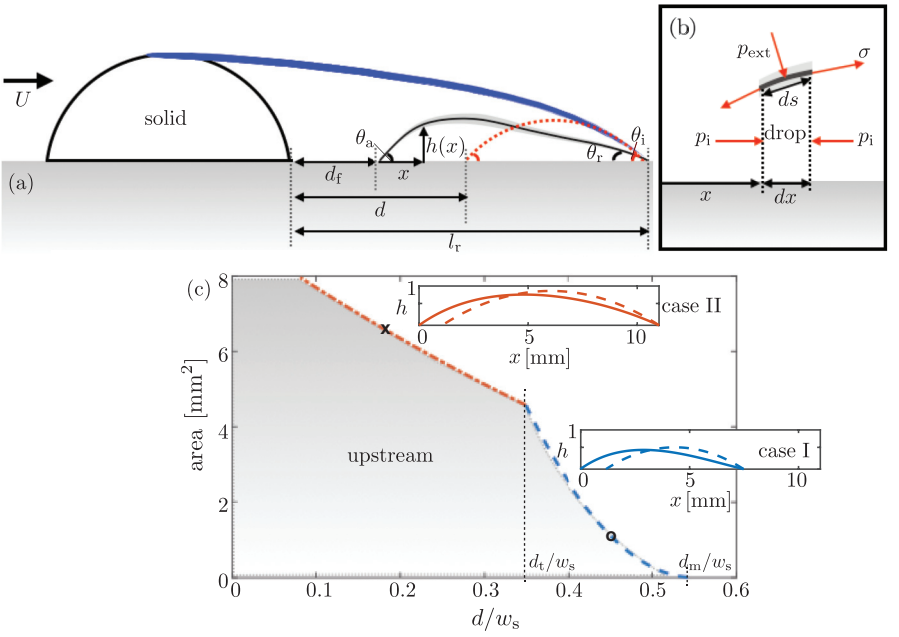

FIG. 4. (a) A 2D schematic of a droplet at the critical onset of depinning upstream when its trailing edge lies at the reattaching point. (b) A schematic of forces acting on a differential element of length, dx, inside the drop. (c) The area of the largest droplet that moves upstream at a given initial distance d/w_s is calculated based on a 2D model in qualitative agreement with the experiments. Here, the droplet is assumed to move upstream when it is completely immersed inside the reattachment zone for both case I and case II. Two droplet shapes (initial: dashed line; final: solid line) for case I ($d/w_s = 0.45$) and case II ($d/w_s = 0.18$) are included. Here the values of the maximum solid-drop distance, $d_m \equiv d(\text{area} \to 0)$, and d_t, the distance that marks the transition between cases I and II, correspond to $d_m/w_s \approx 0.55$ and $d_t/w_s \approx 0.35$.

where ρ_w denotes the density of water, and p_{ext} is the air pressure that interfaces the drop, while σ and g correspond to the surface tension between water and air and the gravitational acceleration, respectively. Analogous to [16], the differential momentum balance requires p_i to be constant and independent of x, which leads to $\partial p_i/\partial x = 0$, or

$$0 = -\sigma h'''(x) + \rho_w g h'(x) + p'_{ext}(x), \tag{3}$$

in the limit of small slope approximations. Presently, we use $\theta_a = 20^\circ$ and $\theta_i = 17^\circ$, which are less than the experimental values, while θ_r is kept at 8.2°.

The key characteristics of the wake behind the solid (i.e., l_r and U) are incorporated into the model through the empirical expression for p_{ext}, which causes the upstream motion of the drop. As we proceed downstream from the solid hemisphere, p_{ext} initially decreases until it reaches the center of vortices in the recirculation zone and then increases again towards the reattachment point [35,36]. Based on the typical pressure values found behind an obstacle [35–38], we model p_{ext} as a parabolic function of x, of which coefficients are found by allowing $p_{ext}(x = l_r - d_f) = p_\infty$ and $\hat{p}^*_{ext} \equiv 2[p_{ext}(x = -d_f) - p_\infty]/\rho_a U^2 = -0.3$. Then, the resultant external pressure gradient, $p'_{ext}(x)$, is given by

$$p'_{ext}(x) = \frac{\rho_a U^2}{2w_s}\left[\frac{\hat{a}}{w_s}\left(x + d_f - \frac{l_r}{2}\right) - \hat{p}^*_{ext}\frac{w_s}{l_r}\right], \tag{4}$$

where the dimensionless empirical parameter, $\hat{a}$, will be presently set to 1, and $l_r = w_s$.

Then, the final governing equation becomes

$$\sigma h''' - \rho_w g h' + \frac{\rho_a U^2}{2 w_s}\left[\frac{1}{5} - \frac{x}{w_s} - \frac{d_f}{w_s}\right] = 0. \tag{5}$$

To compute $h(x)$ that corresponds to case I, Eq. (5) is solved subject to the following boundary conditions:

$$h(0) = 0, \quad h'(0) = \tan\theta_a, \quad h'(l) = -\tan\theta_r, \quad h(l) = 0,$$

where the length of the drop is given by $l = l_r - d_f$. Here, the additional boundary condition is used to compute U that uniquely satisfies the given parameters. For case II, we set $l = l_r$ and replace the third boundary condition with

$$-\tan\theta_i \leqslant h'(l) \leqslant -\tan\theta_r,$$

as the droplet in case II is assumed to reach the solid before the receding angle has evolved to the minimum value. Finally, for each droplet considered, we can calculate its initial distance from the solid, d, by solving for the drop's initial width, w, based on a circular cap shape with the same area:

$$d = l_r - w = l_r - 2\sin\theta_i \sqrt{\frac{\int_0^l h dx}{\theta_i - \cos\theta_i \sin\theta_i}}. \tag{6}$$

The resultant area-d/w_s plot in Fig. 4(c) shows the largest droplet area that will be entrained upstream at a given initial distance from the solid, in good qualitative agreement with the upstream regime of the V-d/w_s phase diagram [Fig. 3(a)]. Comparing with the experimental data, the result for case I captures the relatively steep boundary between upstream and downstream regimes for smaller droplets, while case II qualitatively represents the upper size bound for droplets that fit inside the reattachment zone. Representative droplet profiles for case I ($d/w_s = 0.45$) and case II ($d/w_s = 0.18$) are also included in the insets of Fig. 4(b). In addition, the values of the maximum solid-drop distance, $d_m \equiv d(\text{area} \to 0)$, and d_t, the transitional distance that connects cases I and II, correspond to $d_m/w_s \approx 0.55$ and $d_t/w_s \approx 0.35$ in Fig. 4(c), which reasonably matches the experimental data in Fig. 3(a).

Different values of l_r and p'_{ext} are also incorporated to test the robustness of the present model against empirical values. Specifically, increasing (or decreasing) the value of l_r is observed to increase (or decrease) the size of the upstream regime in Fig. 4(c), as larger l_r signifies that, at given d, a larger droplet can fit within the reattachment length and move upstream, while the overall shape of the regime remains unchanged [see Fig. 6(a)]. Interestingly, increasing the value of $\hat{a}$ decreases the value of d_t [see Fig. 6(b)], as the stronger pressure gradient, or larger $\hat{a}$, ensures that a droplet of given size can now reach the solid before evolving to θ_r (i.e., case II) when placed further away from the solid. However, the overall features of the 2D model remain unchanged by different empirical values used in p'_{ext}; more details of the sensitivity analysis are now included in the Appendix.

This depinning problem involves a complex nonlinear three-dimensional droplet subject to an unsteady turbulent wake behind the solid, and the current 2D droplet model, despite some success, contains a number of significant simplifications that need to be acknowledged here. One such simplification is the small-slope assumption that must break down especially near the advancing edge of the drop. In addition, the pressure inside the wake of the solid and the size of the reattachment zone are assumed to be decoupled from the presence of the droplet and determined completely by U and the geometry of the solid hemisphere alone; hence, we do not presently consider the case in which the droplet is only partially immersed inside the attachment zone and must interact directly with the reattaching flow (which most likely leads to droplet "splitting"). Due to these assumptions, we stress here that the goal of the present 2D model is to capture the *qualitative* trend of the experiments by focusing on the key physical ingredients that lead to the droplet entrainment towards the solid, instead of attempting to *quantitatively* fit the data.

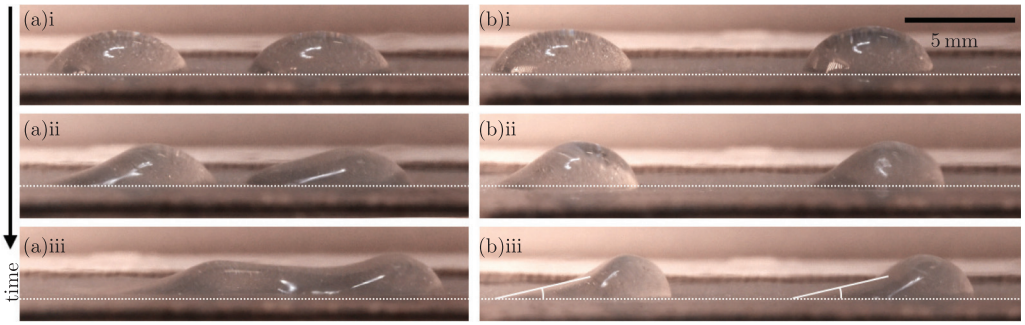

FIG. 5. (a)i Two drops of $V = 50\ \mu$L separated by $d < 1.4w$: Drops deform asymmetrically with imposing wind [(a)ii], and the leader drop is observed to depin before the follower drop and merge with it [(a)iii]. (b)i–(b)iii Droplets of 50 μL at $d > 1.4w$ are observed to deform and depin approximately at the same time.

The key physical mechanism of the upstream motion of the droplet against wind is the droplet immersion inside the reattachment zone behind the solid, wherein the pressure is locally lower than the ambient pressure and the drop remains "shielded" from the wind. In particular, small droplets inside the reattachment region reach the critical depinning configuration (i.e., formation of θ_a and θ_r on the respective edges of the drop), which corresponds to the boundary between the upstream and downstream regimes for small drops in the V-d/w_s phase diagram [Fig. 3(a)]. On the other hand, large drops reach the solid, before forming θ_r, and yield the boundary between the upstream and splitting regimes in Fig. 3(a). The similarity in the overall shape of the upstream regime between the 2D model [Fig. 4(c)] and experiments [Fig. 3(a)] and the robustness of the model against pressure parametrization illustrate the success of the simple model in capturing the key physical mechanism of the droplet depinning towards the solid.

In summary, when high Re wind blows towards a partially wetting drop behind a solid hemisphere with diameter, w_s, the droplet exhibits wake-induced behaviors depending on its distance from the solid, d. When the droplet is placed sufficiently far downstream from the solid (i.e., $d > d_c \approx 1.4w_s$), it depins from the solid substrate and moves downstream at the same critical wind velocity as its no-protrusion counterpart, U_{c0}. When the distance decreases below d_c, the effects of drafting first cause the critical depinning velocity, U_c, to increase above U_{c0}. As d decreases further, "large" droplets are shown to split, as part of the droplet sits inside the recirculation zone behind the solid with suction pressure, while "small" drops move upstream towards the solid leader. The small versus large drops here are determined by their size relative to the recirculation length, l_r. By combining the knowledge of wake behind a rigid body and pinned drop, a simple, 2D droplet model is used to justify the boundaries of the upstream regime in qualitative agreement with the experiments.

The current study with a fixed solid and a droplet can be easily extended to the case of multiple drops pinned on a substrate, which is more directly relevant for aircraft icing and heat exchangers. While having a deformable and moving leader makes the multiple droplet case more complex, preliminary experiments indicate that the depinning behavior of two small drops (i.e., $V = 50\ \mu$L) qualitatively matches the results of the current study. For instance, when the distance between the two drops, d, is less than $d_c \approx 1.4w$, the leader drop depins before the follower, leading to the merging of the two drops that move downstream as one unit, as clearly shown in Fig. 5(aiii). However, for $d > d_c$ [Fig. 5(biii)], the two equal droplets approximately deform and depin at the same time. If a larger droplet (i.e., $V = 150\ \mu$L) is placed upstream of a small drop, the leader drop is observed to reach the follower even for $d > d_c$, in some cases. Having droplets of different sizes brings more complexity into the setup.

This study demonstrates that the incorporation of simple boundary layer concepts can inform the surprising and complex behaviors of a partially wetting drop on a textured surface. While the effect of the wakes generated by moving bodies has been long studied in the high Re locomotion, it has not yet been considered in the context of droplet pinning and depinning, which often occurs in

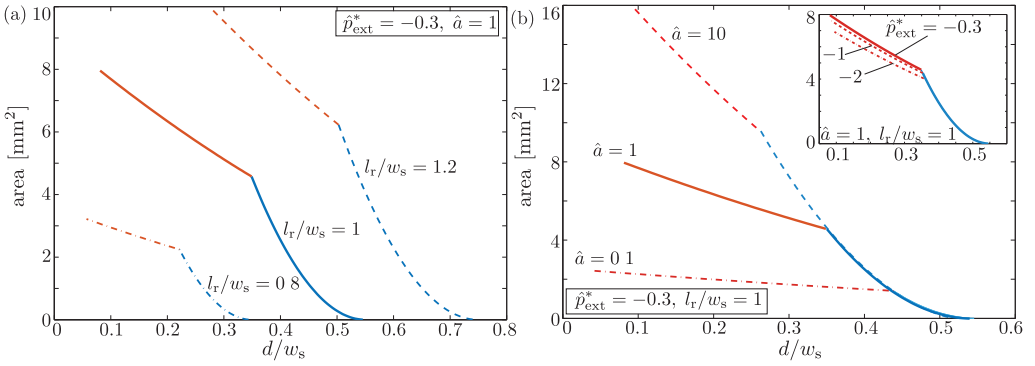

FIG. 6. The area of the largest droplet that moves upstream at a given initial distance d/w_s is calculated based on the 2D model; the reference case from Fig. 4(c) is reproduced here in solid lines, with $l_r/w_s = 1$, $\hat{a} = 1$, and $\hat{p}^*_{ext} = -0.3$. (a) Changing l_r/w_s to 1.2 and 0.8 scales up (down) the overall size of the upstream regime, while the qualitative trend remains unchanged. (b) Varying the pressure gradient inside the reattachment zone by increasing $\hat{a}$ directly decreases d_t and the slope of case II, while the value d_m is unaffected; the inset of (b) shows that further decreasing $\hat{p}^*_{ext}$ slightly reduces the droplet sizes that fit case II.

the high Re regime in aircraft icing and other industrial applications. Furthermore, as much as the existing knowledge of the boundary layer can be used to understand the droplet behavior, simple experiments with droplets can also inform the key characteristics of the boundary layer without the need for sophisticated flow visualization techniques or measurement tools. The combination of the boundary layer and droplet dynamics represents a way of approaching various problems (e.g., atomized lubrication) that lie at the intersection of the two fields.

The authors would like to thank E. White and B. Wilson for helpful discussions; they also acknowledge J. de Bryun for a critical reading of the manuscript. This research was supported in part by NSF (Grant No. CBET-1605947).

APPENDIX: SENSITIVITY ANALYSIS

The main idea behind the 2D model is that the droplet immersed inside the reattachment zone moves upstream against wind due to the negative pressure behind the solid protuberance. Therefore, qualitative characteristics of the upstream regime boundaries must be independent of the specific values of l_r and pressure profile inside the reattachment zone. For instance, the area-d/w_s plot is reproduced in Fig. 6(a) with l_r/w_s set between 0.8 and 1.2, while $\hat{a} = 1$ and $\hat{p}^*_{ext} = -0.3$. Not surprisingly, increasing and decreasing l_r accordingly scales up and down the overall size of the upstream regime; i.e., larger l_r corresponds to a larger droplet that can fit inside the reattachment zone and be entrained upstream at given d/w_s; however, the overall trend remains unchanged. While $l_r = w_s$, which effectively fixes the value of d_m/w_s at 0.55, increasing the pressure gradient inside the reattachment zone (i.e., increasing $\hat{a}$ from 0.1 to 10) directly decreases d_t and increases the corresponding droplet size, as shown in Fig. 6(b). This indicates that a given droplet elongates further and reaches the solid (i.e., case II) when placed at larger d, as the negative pressure gradient to pull the droplet towards the solid becomes stronger. On the other hand, the inset of Fig. 6(b) shows that decreasing the suction pressure behind the solid, $\hat{p}^*_{ext}$, from -0.3 to -2 only slightly reduces the upper boundary of the upstream regime.

[1] A. D. Becker, H. Masoud, J. W. Newbolt, M. Shelley, and L. Ristroph, Hydrodynamic schooling of flapping swimmers, Nat. Commun. **6**, 8514 (2015).

[2] M. M. Zdravkovich, Review—Review of flow interference between two circular cylinders in various arrangements, J. Fluids Eng. **99**, 618 (1977).
[3] J. C. Liao, D. N. Beal, G. V. Lauder, and M. S. Triantafyllou, Fish exploiting vortices decrease muscle activity, Science **302**, 1566 (2003).
[4] D. N. Beal, F. S. Hover, M. S. Triantafyllou, J. C. Liao, and G. V. Lauder, Passive propulsion in vortex wakes, J. Fluid Mech. **549**, 385 (2006).
[5] S. Jung, K. Mareck, M. Shelley, and J. Zhang, Dynamics of a Deformable Body in a Fast Flowing Soap Film, Phys. Rev. Lett. **97**, 134502 (2006).
[6] L. Ristroph and J. Zhang, Anomalous Hydrodynamic Drafting of Interacting Flapping Flags, Phys. Rev. Lett. **101**, 194502 (2008).
[7] P. G. de Gennes, Wetting: Statics and dynamics, Rev. Mod. Phys. **57**, 827 (1985).
[8] D. Quéré, Wetting and roughness, Annu. Rev. Mater. Res. **38**, 71 (2008).
[9] R. J. Kind, M. G. Potapczuk, A. Feo, C. Golia, and A. D. Shah, Experimental and computational simulation of in-flight icing phenomena, Prog. Aero. Sci. **34**, 257 (1998).
[10] T. Cebeci and F. Kafyeke, Aircraft icing, Annu. Rev. Fluid Mech. **35**, 11 (2003).
[11] I. Ghai, J. Wentz, R. E. DeVor, S. G. Kapoor, and J. Samuel, Droplet behavior on a rotating surface for atomization-based cutting fluid application in micromachining, J. Manuf. Sci. Eng. **132**, 011017 (2010).
[12] S. G. Kandlikar and M. E. Steinke, Contact angles and interface behavior during rapid evaporation of liquid on a heated surface, Int. J. Heat Mass Transfer **45**, 3771 (2002).
[13] E. B. Dussan V. and R. Tao-Ping Chow, On the ability of drops or bubbles to stick to non-horizontal surfaces of solids, J. Fluid Mech. **137**, 1 (1983).
[14] E. B. Dussan V., On the ability of drops or bubbles to stick to non-horizontal surfaces of solids. Part 2. Small drops or bubbles having contact angles of arbitrary size, J. Fluid Mech. **151**, 1 (1985).
[15] P. Dimitrakopoulos, Deformation of a droplet adhering to a solid surface in shear flow: Onset of interfacial sliding, J. Fluid Mech. **580**, 451 (2007).
[16] P. A. Durbin, On the wind force needed to dislodge a drop adhered to a surface, J. Fluid Mech. **196**, 205 (1988).
[17] P. Dimitrakopoulos and J. J. L. Higdon, Displacement of fluid droplets from solid surfaces in low-Reynolds-number shear flows, J. Fluid Mech. **336**, 351 (1997).
[18] J. Bico, F. Besselievre, and M. Fermigier, Windswept droplets, in *58th Annual Meeting of the Division of Fluid Dynamics* (American Physical Society, Chicago, IL, 2005).
[19] K. Njifenju, J. Bico, E. Andres, and M. Fermigier, Windswept droplets, in *62nd Annual Meeting of the APS Division of Fluid Dynamics* (American Physical Society, Minneapolis, MN, 2009), Vol. 54.
[20] J. A. Schmucker, Ph.D. thesis, Experimental investigation of wind-forced drop stability, Texas A&M University, 2012.
[21] M. Acarlar and C. Smith, A study of hairpin vortices in a laminary boundary layer. Part 1. Hairpin vortices generated by a hemisphere protuberance, J. Fluid Mech. **175**, 1 (1987).
[22] M. S. Bloor, The transition to turbulence in the wake of a circular cylinder, J. Fluid Mech. **19**, 290 (1964).
[23] J. H. Gerrard, The mechanics of the formation region of vortices behind bluff bodies, J. Fluid Mech. **25**, 401 (1966).
[24] R. Sluder, L. Gris, and J. Katz, Aerodynamics of a generic optical turret, J. Aircraft **45**, 1814 (2008).
[25] E. Savory and N. Toy, Hemispheres and hemisphere-cylinders in turbulent boundary layers, J. Wind Eng. Ind. Aerod. **23**, 345 (1986).
[26] J. S. Wu and G. M. Faeth, Sphere wakes at moderate reynolds numbers in a turbulent environment, AIAA J. **32**, 535 (1994).
[27] T. Maxworthy, Experiments on the flow around a sphere at high Reynolds numbers, J. Appl. Mech. **36**, 598 (1969).
[28] F. M. Najjar and S. P. Vanka, Numerical study of a separated-reattaching flow, Theor. Comput. Fluid Dyn. **5**, 291 (1993).
[29] F. Liang-Shih and K. Tsuchiya, *Bubble Wake Dynamics in Liquids and Liquid-Solid Suspensions* (Butterworth-Heinemann, Stoneham, MA, 1990).
[30] J. E. McDonald, The shape and aerodynamics of large raindrops, J. Meteorol. **11**, 478 (1954).

[31] R. H. Magarvey and R. L. Bishop, Wakes in liquid-liquid systems, Phys. Fluids **4**, 800 (1961).
[32] S. Nogueira, R. G. Sousa, A. M. F. R. Pinto, M. L. Riethmuller, and J. B. L. M. Campos, Simultaneous PIV and pulsed shadow technique in slug flow: A solution for optical problems, Exp. Fluids **35**, 598 (2003).
[33] S. Nogueira, M. L. Riethmuller, J. B. L. M. Campos, and A. M. F. R. Pinto, Flow patterns in the wake of a Taylor bubble rising through vertical columns of stagnant and flowing Newtonian liquids: An experimental study, Chem. Eng. Sci. **61**, 7199 (2006).
[34] J. Faramarzi and E. Logan, Reattachment length behind a single roughness element in turbulent pipe flow, J. Fluids Eng. **113**, 712 (1991).
[35] H. Le, P. Moin, and J. Kim, Direct numerical simulation of turbulent flow over a backward-facing step, J. Fluid Mech. **330**, 349 (1997).
[36] T. A. Johnson and V. C. Patel, Flow past a sphere up to a Reynolds number of 300, J. Fluid Mech. **378**, 19 (1999).
[37] H. J. Kim and P. A. Durbin, Observations of the frequencies in a sphere wake and of drag increase by acoustic excitation, Phys. Fluids **31**, 3260 (1988).
[38] S. Lee, A numerical study of the unsteady wake behind a sphere in a uniform flow at moderate Reynolds numbers, Comput. Fluids **29**, 639 (2000).